JATIS Journal of Astronomical Telescopes, Instruments, and Systems

RESEARCH PAPER

Comparison of polarization aberrations from existing mirror coatings for coronagraphic imaging of habitable worlds

Jaren Nicholas Ashcraft,[a,*] **Brandon D. Dube**,[b] **Ewan S. Douglas**,[c] **Daewook Kim**,[a,c,d] **John E. Krist**,[b] **Bertrand Mennesson**,[b] **Brian Monacelli**,[b] **Rhonda Morgan**,[b] **Nasrat A. Raouf**,[b] **AJ Eldorado Riggs**,[b] **Mike Rodgers**,[e] **and Keith R. Warfield**[b]

[a]University of Arizona, Wyant College of Optical Sciences, Tucson, Arizona, United States
[b]California Institute of Technology, NASA Jet Propulsion Laboratory, Pasadena, California, United States
[c]University of Arizona, Department of Astronomy and Steward Observatory, Tucson, Arizona, United States
[d]University of Arizona, Large Binocular Telescope Observatory, Tucson, Arizona, United States
[e]SYNOPSYS Inc., Pasadena, CA, United States

ABSTRACT. The Habitable Worlds Observatory (HWO) aims to directly image and spectroscopically characterize Earth-like exoplanets. This may be done with a coronagraph instrument, which can suppress the host star's light by a factor of $\sim 10^{10}$. One of the key factors limiting the performance of these instruments at that level is the aberration of the wavefront due to polarization. Changes in the angle of incidence across a beam result in spatially varying polarization state changes called polarization aberrations. Polarization aberrations present a unique problem in high-contrast imaging because the orthogonally polarized components of the wavefront experience different aberrations. This means that standard wavefront control techniques will be incapable of removing the aberration from all polarizations simultaneously. We report on the influence of polarization aberrations for an early-concept study in support of the HWO called the Six Meter Space Telescope operating with two different Apodized Pupil Lyot Coronagraph designs, which we developed for this study. Polarization aberrations from three different coatings studied set a mean uncompensated normalized intensity between 1 and 10×10^{-10} at the inner working angle. To minimize the influence of polarization aberrations, we split the coronagraph into orthogonal polarization channels and control the mean wavefront incident on each channel separately. This reduces the intensity at the inner working angle by an order of magnitude, restoring 10^{-10} contrast. We then outline strategies for further compensation of polarization aberrations that can be considered in future work.

 [DOI: 10.1117/1.JATIS.11.1.015002]

Keywords: high-contrast imaging; polarization; polarization aberration; coronagraphy; coatings

Paper 24133G received Aug. 27, 2024; revised Dec. 2, 2024; accepted Dec. 27, 2024; published Jan. 29, 2025.

1 Introduction

1.1 High-Contrast Imaging Goals for the Habitable Worlds Observatory

The pathways to discovery in Astronomy and Astrophysics Decadal survey for 2020 has identified the strategic importance of direct exoplanet imaging to science in the coming coatings

*Address all correspondence to Jaren Nicholas Ashcraft, jarenashcraft@ucsb.edu

decade. Toward this end, next-generation observatories on the ground and in space will be equipped with instrumentation capable of imaging faint stellar companions at small angular separations with respect to their host star. These coronagraphic instruments employ specialized masks and wavefront sensing and control (WFSC) systems to reject the starlight from the focal plane and destructively interfere with the starlight in a high-contrast region on the focal plane called a "dark hole." These instruments must be capable of imaging exoplanets in reflected light at high contrasts ($\approx 1 \times 10^{-10}$) and small angular separations ($\approx$100 mas).[1] However, at contrasts this high, the coronagraph is sensitive to effects that have not been a limiting factor in prior missions.[2] One such effect results from the change in the angle of incidence across a beam, which introduces spatially varying changes in the polarization state. This effect, called polarization aberration, results in both phase and amplitude aberrations that differ for orthogonal polarization states.

NASA's Jet Propulsion Laboratory (JPL) has produced a conceptual design traceable to the goals of the proposed Habitable Worlds Observatory (HWO) for an observatory and suite of instruments including a coronagraph. Dubbed the Six Meter Space Telescope (6MST),[3] it features a segmented 6-m diameter primary mirror as part of an unobscured four-mirror optical telescope assembly (OTA). The coronagraph is offset within the field of view and features its own small tertiary (M3) and quaternary (M4). Following these optics are two twin coronagraphs, separated by a polarization beamsplitter. The 6MST OTA and one of the twin coronagraphs are shown in Fig. 1.

The 6MST has been designed to minimize the influence of polarization effects on the performance of the coronagraph instruments by maintaining small angles of incidence. The design features a maximum angle of incidence of 15 deg in the OTA where polarization aberrations predominantly arise. The off-axis parabolas (OAPs) that make up the coronagraph have slow F-numbers and are minimally off-axis to minimize the change in angle of incidence across the beam when incident on an OAP. Understanding the design's polarization effects is critical to understanding the best achievable contrast with its coronagraphs.

1.2 Polarization Aberrations

Polarization aberrations are a physical optics phenomenon that has recently gained attention in the high-contrast imaging community due to their potential to limit observations of Earth-like exoplanets.[4] The goal of directly imaging exoplanets in reflected light at small angular separations is extremely sensitive to aberrations, which cause light to leak into the coronagraph's focal plane. Polarization aberrations are typically small in comparison to scalar wavefront aberrations that arise from misalignment or optical surface errors but largely manifest as phase and amplitude aberrations with the same geometry as second- and third-order aberrations (tilt, defocus, astigmatism) that vary as a function of polarization.[4] The fundamental theory of polarization

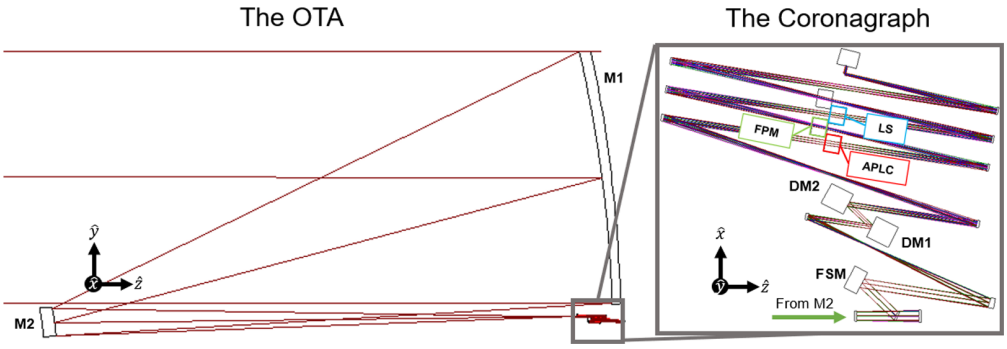

Fig. 1 6MST optical design, featuring a 6-m diameter, off-axis, segmented primary mirror as a part of a four-mirror OTA. 6MST features twin coronagraphs, one of which is shown on the right of this figure in a zoomed-in view. The coronagraph features a fast-steering mirror (FSM) for pointing and jitter control, two deformable mirrors (DM1, DM2) for high-order wavefront sensing and control, and two image and pupil planes for coronagraph masks, field stops, and/or filters. The locations for the APLC pupil mask, focal plane mask (FPM), and Lyot Stop (LS) used in this study are highlighted in red, green, and blue on the coronagraph diagram, respectively.

aberration was derived by McGuire and Chipman,[5,6] and an alternative interpretation based on plane-symmetric optical systems was developed by Sasián.[7] Breckinridge et al.[4] discussed polarization in the context of high-contrast imaging by studying the impact on the point-spread function (PSF). Polarization aberrations were a design constraint for the Habitable Exoplanet Observatory (HabEx) mission concept that limited the focal ratio of the primary mirror to F/2.5.[8] Will and Fienup[9] found that polarization aberrations severely degrade contrast near the inner working angle (IWA) of the proposed coronagraph architectures for the Large UV/Optical/IR Surveyor (LUVOIR) mission concept, particularly at shorter wavelengths. Recently, Anche et al.[10] found that polarization aberrations in the future ground-based 30-m class telescopes suffer from polarization aberration limiting performance near the IWA to $10^{-6} - 10^{-5}$ contrast in the IR and worse performance at shorter wavelengths. Balasubramanian et al.[11] showed that optimized mirror coatings for the proposed Terrestrial Planet Finder Coronagraph could mitigate the influence of polarization aberrations from the telescope. Based on the observations made in the literature, polarization is a known limiter to high-contrast imaging efforts and must be considered for the HWO mission concept to optimize direct exoplanet detection.

1.3 Polarization Ray Tracing and the Jones Pupil

To optimize the polarization aberrations present in a system, we must first be able to model them. Polarization ray tracing (PRT) is an integral tool in the analysis of an optical system's polarization aberrations. From a PRT model, one can construct the Jones pupil, which encodes the polarization-dependent response of an optical system's exit pupil. We refer readers interested in the exact mechanics of this technique to the extensive literature that covers its implementation.[12–14] The basic principle of PRT is to represent each surface in an optical system by a 3×3 PRT matrix $\mathbf{P}_q$, which is composed of a diagonal matrix $\mathbf{J}_q$ and two orthogonal transformation matrices $\mathbf{O}_{\text{in}}$ and $\mathbf{O}_{\text{out}}$, as shown in Eq. (1)

$$\mathbf{P}_q = \mathbf{O}_{\text{out}}\mathbf{J}_q\mathbf{O}_{\text{in}}^{-1} = \mathbf{O}_{\text{out}}\begin{pmatrix} r_{s,q} & 0 & 0 \\ 0 & r_{p,q} & 0 \\ 0 & 0 & 1 \end{pmatrix}\mathbf{O}_{\text{in}}^{-1}, \tag{1}$$

where $\mathbf{J}_q$ contains the complex reflection coefficients for the light-matter interaction at the q'th surface, and the orthogonal transformation matrices describe the rotation into ($\mathbf{O}_{\text{in}}$) and out of ($\mathbf{O}_{\text{out}}$) the coordinate system defined by the basis vectors, which describe a rotation into and out of the local coordinates of the surface. The optical system can then be represented by a matrix product of these PRT matrices, shown in Eq. (2)

$$\mathbf{P}_{\text{tot}} = \prod_{q=1}^{Q}\mathbf{P}_q = \mathbf{P}_Q \ldots \mathbf{P}_2\mathbf{P}_1. \tag{2}$$

The resulting $\mathbf{P}_{\text{tot}}$ matrix represents the three-dimensional transformation of any polarization state in the entrance pupil to the exit pupil in global coordinates. To analyze the influence on the PSF of optical systems, we must transform the PRT matrix into the local coordinates of the exit pupil of the instrument we want to analyze. This procedure is covered exhaustively in chapter 11 of Chipman et al.,[14] so the interested reader should review the method and choice of coordinate system there. The local coordinate transformation is achieved by deriving the orthogonal transformations for the entrance pupil (EP) and exit pupil (XP), and the application of Eq. (3) will yield the final Jones pupil $\mathbf{J}_{\text{tot}}$

$$\mathbf{J}_{\text{tot}} = \mathbf{O}_{\text{XP}}^{-1}\mathbf{P}_{\text{tot}}\mathbf{O}_{\text{EP}}. \tag{3}$$

To analyze the polarization aberrations of the Jones pupil, we can examine its eigenvalues Λ_s, Λ_p, given by Eq. (4)

$$\Lambda_s = A_s e^{i\phi_s}, \;\; \Lambda_p = A_p e^{i\phi_p}. \tag{4}$$

The eigenvalues of the Jones pupil are representations of the complex amplitude that orthogonal polarization states experience by interacting with the surface. The polarization-dependent phase aberrations are described by retardance [δ, shown in Eq. (5)] and given by the difference in phase between the eigenvalues of $\mathbf{J}_{\text{tot}}$. Retardance describes the phase delay between the orthogonal eigenpolarizations of a given beam

$$\delta = \phi_s - \phi_p, \tag{5}$$

where ϕ_s and ϕ_p are the phases of orthogonal s- and p-polarizations, respectively. The amplitude aberrations are described by diattenuation [D, shown in Eq. (6)]

$$D = \frac{A_s^2 - A_p^2}{A_s^2 + A_p^2}. \tag{6}$$

where A_s and A_p are the amplitudes of orthogonal s- and p- polarizations, respectively. The effects of diattenuation and retardance have been studied in the context of astronomical telescopes recently due to their potential to limit high-contrast imaging.[4,9,10] Several strategies have been proposed for how to compensate for polarization aberrations in optical systems. Maintaining low angles of incidence is the simplest method of mitigating polarization aberrations, but this limits the primary mirror diameter subject to a given observatory packaging constraint and reduces the stability of the observatory by placing the secondary mirror on a long, flexible support. The design of a pupil-plane spatially varying retarder plate was proposed by Clark and Breckinridge,[15] which was a complex device composed of a stack of isotropic and birefringent materials. Balasubramanian et al.[11] showed with coronagraphic physical optics models that it is possible to select for a coating with the least contrast degradation, but they found that ultimately contrast at separations $<2\lambda/D$ was limited by polarization aberration.

1.4 Goals of This Study

In this work, we aim to demonstrate an open-source integrated modeling framework capable of assessing how polarization aberrations degrade the contrast of a coronagraph onboard an off-axis 6-m space telescope. We use the 6MST optical design to produce the polarization aberrations that we propagate through an Apodized Pupil Lyot Coronagraph (APLC) physical optics model. We can then use this modeling framework to identify strategies that enable 10^{-10} contrast near the coronagraph's IWA. Using integrated physical optics modeling of polarization and diffraction, this study will determine if the proposed split coronagraph design for 6MST with orthogonal polarization channels is sufficient to mitigate polarization aberrations in the visible.

In Sec. 2, we review the open-source software platforms used to perform the simulations of polarization aberration and diffraction. We also discuss a novel design method for APLCs that was developed to produce the coronagraphs analyzed in this study. In Sec. 3, we show the nominal response of the APLCs subject to the polarization aberrations from three different coatings. In Sec. 4, we assess the performance of the dual-channel coronagraph with WFSC. In Sec. 5, we review this study and discuss emerging technologies that may be able to best address polarization aberration.

2 Methods

The 6MST design features an F/2.5 primary mirror as part of an unobscured, off-axis design. The coronagraph instrument (CI) uses an offset field, which allows it to be positioned "under" the primary mirror (as shown in the grey box in Fig. 1) rather than a more conventional instrument bay position, such as behind the primary mirror. This is intended to reduce the influence of polarization aberrations by keeping angles of incidence low. The CI itself features two deformable mirrors, a transmissive pupil apodizer location, a focal plane mask position, Lyot stop position, and field stop position. At the fore is a fast steering mirror, which will be used to perform precision pointing and line of sight control. The CI is divided into two twin channels, split by a polarization beamsplitter. Although the 6MST design utilized a "keystone" segmentation approach, we have designed APLCs based on the hexagonal segmentation architecture specified by the Ultra-Stable Observatory Roadmap Team.[16]

Our physical optics modeling is conducted using two open-source physical optics packages in Python. We conduct the simulation of Jones pupils using Poke.[17] Poke is an open-source ray-based physical optics platform that translates ray data from commercial ray tracers (CODE V, Zemax OpticStudio) into a Python environment utilizing the ray tracer's Python API. Poke can then carry out the three-dimensional PRT calculus described earlier in Sec. 1 (also in chapter 9 of Chipman et al.[14]) to simulate the Jones pupil in Python. For diffraction simulation, we use the

open-source numerical optics package prysm, which provides rapid diffraction simulation that is capable of the large-scale iterative simulations needed to design coronagraphs in a short period. Algorithmic differentiation is also included for the propagation routines, which facilitates coronagraph optimization.

2.1 Design of an Apodized Pupil Lyot Coronagraph

The fiducial coronagraph for this study is an APLC with an annular dark hole. We choose the APLC as a motivating example in this study because of its importance in NASA Astrophysics missions. The soon-to-launch Roman Coronagraph features two APLC (called shaped pupil coronagraphs, or SPCs) modes for direct imaging and spectral characterization.[18] Furthermore, the baseline coronagraph architecture for the LUVOIR-A mission concept was an APLC.[19] Understanding the response of APLCs to polarization aberrations will be beneficial to future studies in support of HWO.

To design the APLCs used in this study, the focal plane mask and Lyot stop were manually specified; then, a grayscale apodizer M was designed via constrained nonlinear optimization. The scalar loss function $\mathcal{L}$ was defined to be the sum of the intensity in the dark hole

$$\mathcal{L} = \sum_{\lambda_i=\lambda_1}^{\lambda_N} \sum_{p=1}^{\mathrm{DH}} I(\lambda_i, p), \tag{7}$$

where λ_i is a wavelength spanning $\lambda_1 - \lambda_N$, and p is the index of a pixel in the dark hole. $\mathcal{L}$ does not contain a penalty for lost throughput. This could be improved in the future. One can also adjust the core of the loss function to, for example, $(I - 10^{-10})$ to drive the intensity to a specific value. Gradient back-propagation rules as described by Jurling and Fienup[20] were used to compute the partial derivative of $\mathcal{L}$ with respect to each pixel of the grayscale apodizer, $\partial\mathcal{L}/\partial M$. The back-propagation logic is implemented within prysm and dygdug,[21] which is an extension of prysm dedicated to coronagraphy. Prysm's optimization module contains numerous gradient-based optimizers; to constrain the apodizer to values between 0 and 1, we used the L-BFGS-B optimizer,[22,23] which supports exact box constraints.

We perform mask optimization at 1024×1024 resolution, using five discrete wavelengths centered on λ_0 of 656 nm that span a $10\%\lambda_0$ bandpass. For this study, we designed two coronagraphs to the specifications outlined in Table 1.

The resulting coronagraphs utilize a grayscale apodizer. We make no additional constraints outside of the nominal performance for manufacturability. The conversion of grayscale apodizations to binary designs to be viable in fabrication is outside the scope of this work but has been

Table 1 Coronagraph design specifications for the two APLCs used in this study. We consider an APLC whose dark hole spans $3.5 - 12\lambda/D$ to match the dark zone of the APLC for the LUVOIR-A ECLIPS coronagraph.[19] To study effects at smaller IWA, we also design an APLC whose dark hole spans $2.5 - 10\lambda/D$. The only difference in these specifications is the IWA, which is highlighted in bold.

Specification	Value (APLC-3.5)	Value (APLC-2.5)
Aperture (D)	6.51-m entrance pupil	6.51-m entrance pupil
Segment flat-to-flat distance	1559 mm	1559 mm
Segment gap size	18.75 mm	18.75 mm
Field of view	**3.5–12** λ/D	**2.5–12** λ/D
Center wavelength (λ_o)	656 nm	nm
Bandwidth	65.6 nm ($10\%\lambda_o$)	65.6 nm ($10\%\lambda_o$)
Nominal mean NI	$\approx 10^{-11}$	$\approx 10^{-11}$
Lyot stop diameter	$\%D$ 90	$\%D$ 90

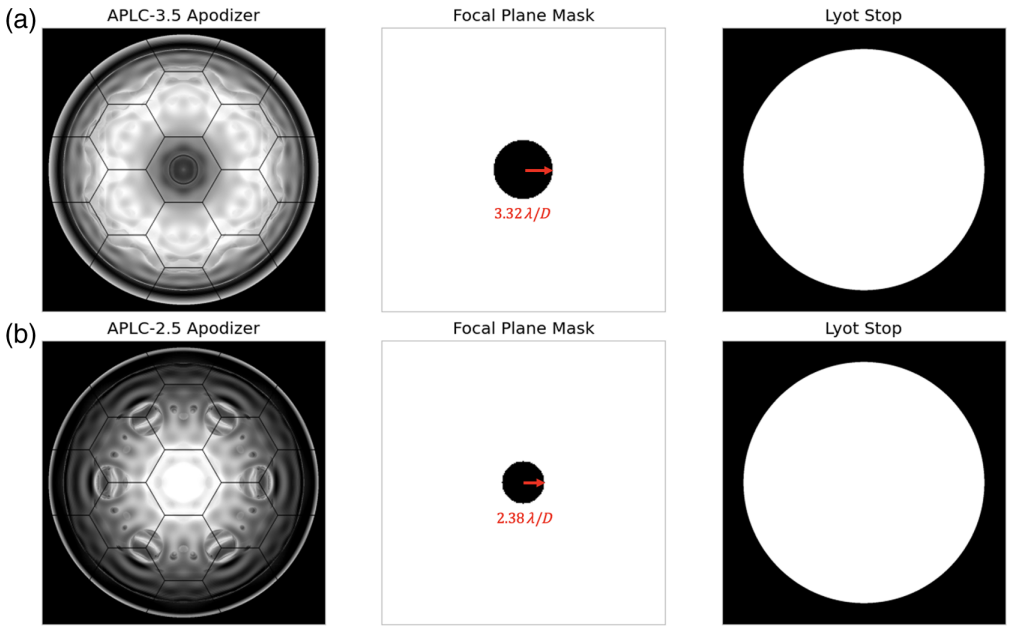

Fig. 2 Illustration of the APLCs designed for the hexagonal segment architecture. These coronagraphs use a simple binary occulter for a focal plane mask and a Lyot stop that is 90% of the diameter of the full entrance pupil. Panel (a) shows the APLC-3.5 design, with a $3.5\lambda/D$ IWA, and panel (b) shows the APLC-2.5 design, with a $2.5\lambda/D$ IWA. The FPM is undersized slightly to allow for a margin between the FPM and the beginning of the dark hole, which occurs at $2.5\lambda/D$ and $3.5\lambda/D$.

investigated elsewhere (e.g., Martinez et al.[24]). Grayscale apodized masks for vortex coronagraphs behind segmented apertures have been demonstrated by depositing gold microdots to approximate the continuous profile.[25] Our APLC designs are shown in Fig. 2.

The $3.5\lambda/D$ IWA APLC is henceforth called "APLC-3.5," and the $2.5\lambda/D$ IWA coronagraph is henceforth called "APLC-2.5." Note that the dark hole optimization target is the field of view specification in Table 1, but to satisfy these constraints, the FPM is undersized slightly, such that their radii are equal to 2.5 and $3.5\lambda/D$ at the shortest wavelength in the band. The FPM radii are shown in terms of the center wavelength in Fig. 2. This enables the margin between the FPM and the dark hole, where light spreads as a consequence of the chromatic scaling of the point-spread function.

To achieve the nominal mean NI specification, each broadband optimization required 3000 iterations (15000 iterations of monochromatic optimization), which required 45 min of GPU runtime or ≈5 iterations per second. In Fig. 3, we evaluate the throughput and normalized intensity (NI) of these coronagraphs as a function of angular separation. Here, NI is defined as the intensity at the coronagraphic focal plane divided by the peak intensity of the coronagraphic focal plane with the focal plane mask removed. We observe a core ($r < 0.7\lambda/D$) throughput of 21.2% for the APLC-3.5 design and 12.3% for the APLC-2.5 design. The APLC's trade of throughput for IWA is well known[26] and is an inevitable consequence of using amplitude apodization coronagraphs.

2.2 Coating Formulas

To simulate the polarization aberrations for this study, we consider a few established coating equations. We first employ the enhanced lithium fluoride–protected aluminum (Al_{eLiF}) coating described by Fleming et al.[27] Al_{eLiF} has appreciable reflectivity in the far ultraviolet, which is desirable for HWO science, and enhanced environmental durability to ensure performance over a long mission lifetime. For comparison, we also consider a magnesium fluoride–protected aluminum coating similar to that used on the Hubble Space Telescope (Al_{HST}), and a protected Silver coating (Ag_{Prot}) that is not particularly optimized for HWO science but features more dielectric layers. The refractive indices for the materials used in this study are given in Table 2.

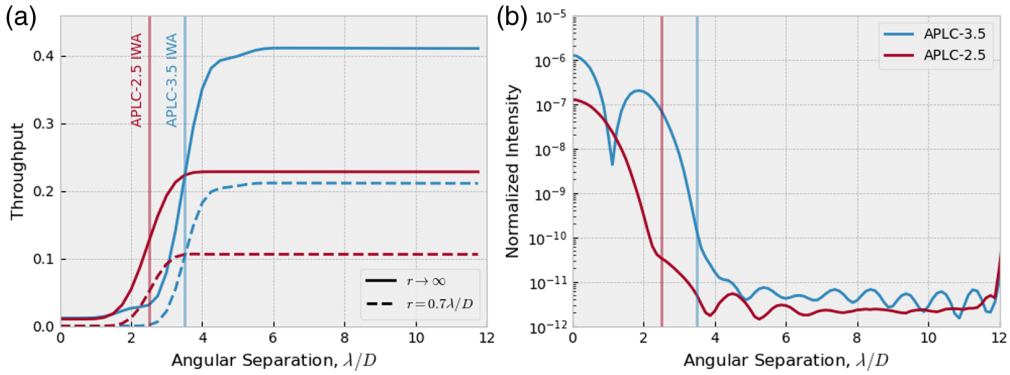

Fig. 3 (a) Throughput versus angular separation for the APLC-3.5 and APLC-2.5 designs. Here, throughput is defined as the ratio of the total intensity observed at the coronagraph focal plane versus the total intensity at the unapodized pupil plane. The dashed line shows the core throughput, or the throughput within a $0.7\lambda/D$ radius centered on the core. We observe that for these designs, roughly a factor of 2 of throughput is lost by pushing to an IWA that is $1\lambda/D$ shorter. We also note that the core $0.7\lambda/D$ contains about 50% of the total intensity for both coronagraphs. (b) The azimuthal average of the focal plane intensities in units of normalized intensity (NI), defined by dividing the intensity of the coronagraphic focal plane by the peak intensity with the mask removed. The actual NI at the IWA is $\sim 3 \times 10^{-11}$ and 2×10^{-10} for the APLC-2.5 and APLC-3.5, respectively.

Table 2 Complex refractive indices for the materials used in this study, and their reference as given by refractiveindex.info. The sign convention for the refractive index is chosen to be consistent with the multilayer thin-film algorithm used in *Poke*, as shown by Peatross and Ware,[28] where the complex index = $n + ik$.

Material	Refractive index at $\lambda = 656$ nm	Reference
LiF	1.3909	Li[29]
MgF_2	1.4208 + 0.00052032i	de Marcos et al.[30]
SiO_2	1.4715	Gao et al.[31]
Ta_2O_5	2.131306	Gao et al.[32]
Si_3N_4	2.0078	Philipp[33]
Al	0.94244 + 6.2747i	Cheng et al.[34]
Ag	0.074 + 4.113i	Ciesielski et al.[35]
Fused silica	1.4564	Malitson[36]

The recipes for the coatings used in this study are given in Table 3, and their spectral reflectivity is shown in Fig. 4. The responses of the aluminum-based Al_{eLiF} and Al_{HST} are very similar. This similarity in performance is owed to their simplicity, both being composed of a single thin dielectric layer over aluminum. The Ag_{Prot} coating is more complicated, being composed of three dissimilar dielectric materials deposited on silver. Ag_{Prot} is not a candidate coating considered in the 6MST study but is used as a comparison to illustrate the influence of more dielectric layers on polarization aberrations. The Ag_{Prot} coating is used for the internal coronagraph imaging optics and fold mirrors to maximize transmission in the visible and near-IR. The deformable mirrors (DM1, DM2) will be treated as an aluminum substrate for the purposes of this study.

To ground the coatings in the context of the polarization aberrations discussed in Sec. 1, we evaluate the diattenuation and retardance for the coatings in Table 3 at our chosen center wavelength for a range of angle of incidences from 0 to the maximum angle in the optical path leading up to the coronagraph. The results are shown in Fig. 5. These data suggest that the aluminum-based coatings at this wavelength will experience a greater degree of diattenuation, and all three

Table 3 Mirror coating recipes analyzed in this study. The order is such that light encounters layer 1 first, propagates to the substrate, and then reflects back through the thin film stack. The substrate is treated as fused silica for completeness in our simulations, but the reflective metal layer 4 for each coating is sufficiently thick that it can be treated as the substrate at these wavelengths.

	Al_{eLiF}	Al_{HST}	Ag_{Prot}
Layer 1	N/A	N/A	60-nm SiO_2
Layer 2	N/A	N/A	62-nm Ta_2O_5
Layer 3	17-nm LiF	25-nm MgF_2	50-nm Si_3N_4
Layer 4	70-nm Al	100-nm Al	1600-nm Ag
Substrate	Fused silica	Fused silica	Fused silica

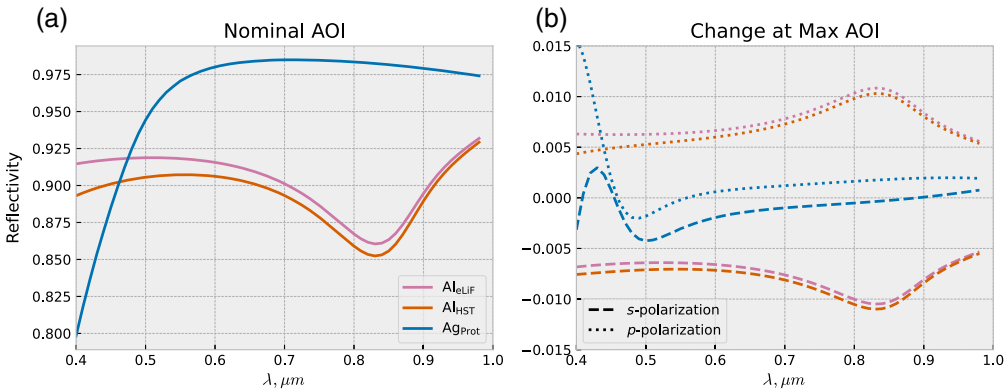

Fig. 4 Comparison of the spectral reflectivity of the coating formulas described in Table 3. On panel (a), we show the reflectivity as a function of wavelength for light that is normally incident on a mirror substrate. On panel (c), we show the polarization-dependent change in reflectivity over the same spectral range. We observe that the Al_{eLiF} and Al_{HST} coatings have an approximately symmetric splitting of the *s*- and *p*-polarization's reflectivity. The protected Ag recipe on the other hand lacks this symmetry, with a low change in reflectivity across the spectral band except for in the near ultraviolet.

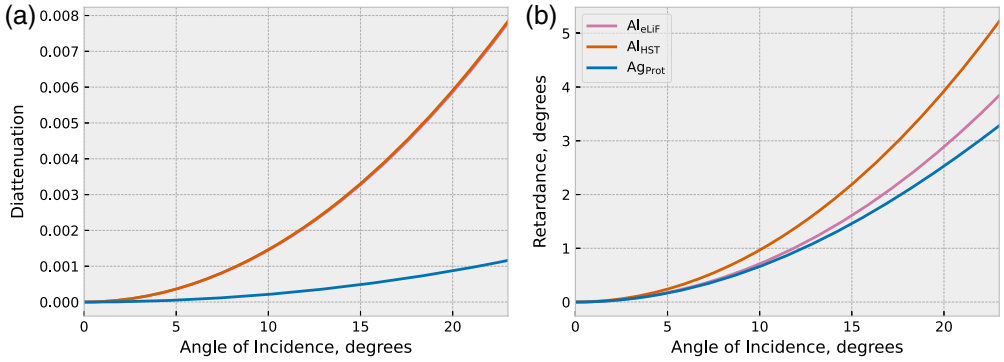

Fig. 5 Comparison of the diattenuation (a) and retardance (b) as a function of the angle of incidence in the observatory evaluated at $\lambda = 656$ nm. The aluminum-based coatings are much stronger diattenuators, which is consistent with the results of Anche et al.[10] who studied an aluminum coating for the GMT. The extinction coefficient of aluminum is much higher than silver at this wavelength, so the higher diattenuation is to be expected. The retardance of all three coatings follows a similar trend, with the Al_{HST} coating being the greatest retarder, and the Ag_{Prot} coating being the least.

coatings experience similar levels of retardance, with the Al_{HST} coating experiencing the largest retardance. However, these are not quantities that directly inform how well an imaging system performs. We must construct a physical optics model of the coronagraph and subject it to polarization aberrations to precisely understand the influence on the focal plane.

3 Nominal Results

We begin by evaluating the polarization aberrations of the 6MST system immediately before the coronagraph, located after DM2. We do so because we are interested in sources of wavefront error that cause leakage of starlight into the coronagraph's dark hole. The coronagraph vignettes the majority of the starlight, so the optics after the coronagraph do not result in meaningful stellar leakage. Using Poke, we perform a PRT simulation to generate a Jones pupil (**J**) for each coating specified in Table 3. A different **J** is computed for each wavelength across the 10% bandwidth centered on $\lambda_0 = 656$ nm. The resulting elements of **J** are parameterized to the Zernike polynomial basis such that they are independent of spatial sampling, following the approach used to model polarization aberrations in the Roman Coronagraph by Krist et al.[2] The resulting Jones pupil for the Al_{eLiF} coating evaluated at λ_0 is shown in Fig. 6.

The remaining Jones pupils for the Al_{HST} and Ag_{Prot} coatings can be found in Appendix B. We show the uncompensated Jones pupils to illustrate their total contribution to the wavefront error budget, which is shown as an RMS amplitude and phase error in Table 4. These data suggest that the Al_{HST} coating contributes the greatest amount of amplitude aberration, and the Ag_{Prot} coating contributes the greatest amount of phase aberration of the three coatings studied.

Using prysm, we can then propagate the elements of **J** individually through the coronagraph to arrive at the focal plane representation of the Jones matrix. This is referred to as the amplitude response matrix ($\mathbf{ARM}(x', y')$) of the system. To accurately compute the focal plane intensity (I) that would be detected from an electric field described by **J**, one would generally need to convert **ARM** into a Mueller matrix. The Mueller matrix analog of **ARM** is referred to as the Mueller point-spread matrix [$\mathbf{MPSM}(x', y')$].[14,38] However, in response to an unpolarized point source, the only relevant contribution of this matrix is the $\mathbf{MPSM}_{0,0}$ element or the top left element of the **MPSM**. The form of this element is known as a function of the elements of the Jones pupil and given in Eq. (8)

$$I(x', y') = \mathbf{MPSM}_{0,0}(x', y') = \frac{1}{2}\sum_{j=1}^{2}\sum_{k=1}^{2}|\mathbf{ARM}_{j,k}(x', y')|^2. \tag{8}$$

where j and k are the row and column indices of **ARM**, respectively.[37] The results of this propagation for the coatings studied are shown in Fig. 7. These data are the result of applying no

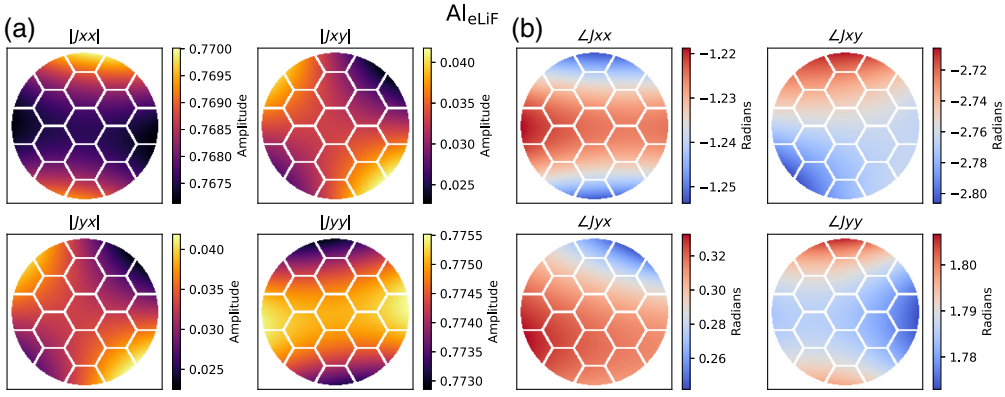

Fig. 6 Uncompensated Jones pupils for the Al_{eLiF} coating on M1 and M2 of 6MST evaluated before the coronagraph focal plane mask. Panel (a) is the amplitude of the complex Jones pupil, which is dimensionless, and panel (b) is the phase in radians. The Jones pupil was computed in the local x/y coordinate system of the 6MST coronagraph. We remove the apodizer from these data to show the underlying structure of the polarization aberration, which is dominated by astigmatism and tilt-like terms.

Table 4 RMS amplitude [Fig. 6(a)] and phase [Fig. 6(b)] errors for the coatings analyzed in this study. Each value in this table corresponds to an element of a Jones pupil. For example, the top-right box contains the RMS phase errors for the Al_{eLiF} Jones pupil, where the order of the values corresponds to the phase maps in Fig. 6. The amplitude values are given with their mean to indicate their relative influence on the focal plane intensity. We subtract the mean value of each Jones pupil element when computing the RMS because constant amplitude and phase do not influence coronagraphic contrast.

Coating	Mean amplitude ± RMS error (%)		RMS phase error (nm)	
Al_{eLiF}	76.82 ± 0.05	3.289 ± 0.288	0.69	1.764
	3.284 ± 0.293	77.442 ± 0.048	1.606	0.519
Al_{HST}	76.118 ± 0.054	3.259 ± 0.374	1.079	1.769
	3.254 ± 0.380	76.732 ± 0.047	1.883	0.534
Ag_{Prot}	83.062 ± 0.018	3.562 ± 0.291	1.952	1.61
	3.551 ± 0.296	83.846 ± 0.014	2.568	1.017

wavefront control and not splitting the coronagraph into orthogonal polarization channels, which we will consider in Sec. 4.

Figure 7 shows the science focal planes of the APLC-3.5 and APLC-2.5 coronagraphs subject to the polarization aberrations from the Al_{eLiF}, Al_{HST}, and Ag_{Prot} coatings. Qualitatively, the nominal wavefront error looks remarkably astigmatic, with a clear nearly vertical axis in which the stellar leakage is worst. It is also very apparent that the Ag_{Prot} coating underperforms compared with the aluminum-based coatings. This trend follows the order of the RMS phase error in Table 4. For a more quantitative comparison, we compute the azimuthally averaged radial profiles of the data in Fig. 7. The results are shown in Fig. 8. We observe that the Ag_{Prot} coating contributes the largest nominal degradation in NI, whereas the Al_{eLiF} and Al_{HST} coatings degrade the contrast substantially less. In Table 5, we report on the fractional change in NI (or ΔNI) equal to the NI at the IWA for the aberrated divided by the nominal case. Here, we observe that the

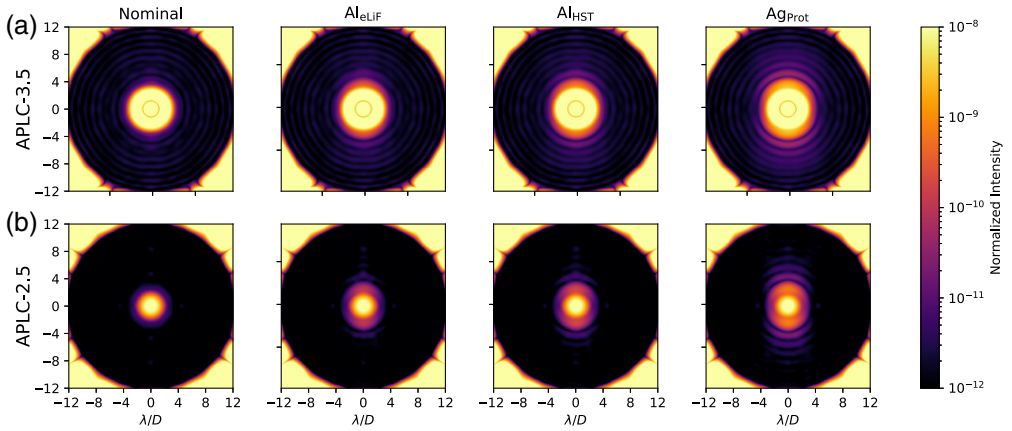

Fig. 7 Focal plane response of the APLC-3.5 (a) and APLC-2.5 (b) to polarization aberrations from the coatings denoted by the column title. The leftmost "nominal" column is the focal plane intensity without polarization aberrations. Polarization aberrations are of low spatial order, so intensity leakage on the coronagraphic focal plane is concentrated near the IWA. The structure of the aberration is highly directional and indicative of the on-axis astigmatism that is typical of polarization aberrations in astronomical telescopes.[4] The eLiF and HST coatings perform very similarly, with prominent features 2 to 12 times brighter than the nominal NI appearing near the IWA. The pAg coating contributes roughly an order of magnitude more, with the dominant degradation at the IWA being closer to 10 to 40 times the nominal NI.

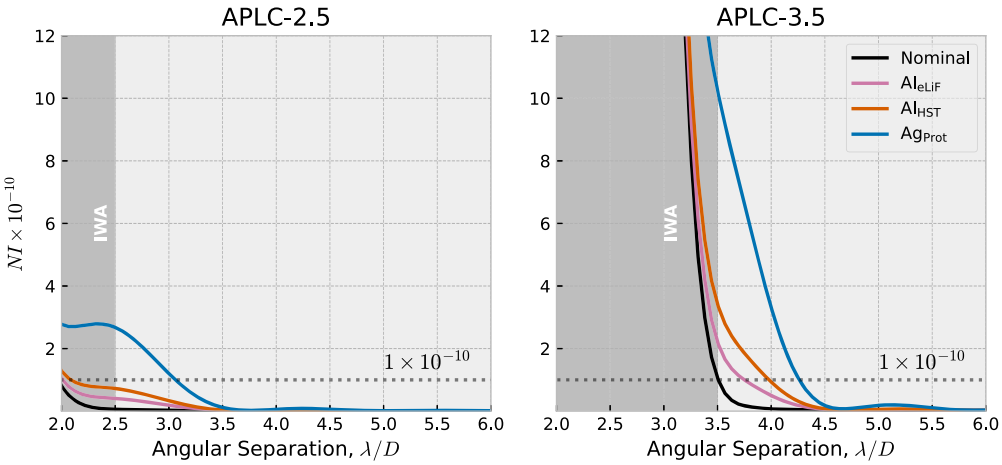

Fig. 8 Azimuthally averaged radial profiles of the NI from the aberrated cases shown in Fig. 7. At first glance, these data may appear to suggest that the APLC-3.5 is more sensitive to polarization. However, as we note from Fig. 3, the contrast at the IWA of APLC-3.5 begins nearly an order of magnitude higher than the APLC-2.5. With this in mind, the two coronagraph's sensitivity to polarization is more comparable. The pAg coating contributes the highest nominal NI degradation, whereas the eLiF and HST coatings contribute substantially less degradation at the IWA.

Table 5 Ratio of the observed NI at the IWA for the aberrated case versus the nominal case. As the nominal contrast of the APLC-2.5 at the IWA is higher, the change is more significant. The order of "best" performing to "worst" performing is predicted by the RMS phase error column of Table 4.

Coating	Al_{eLiF}	Al_{HST}	Ag_{Prot}
APLC-3.5 ΔNI	2.15	3.36	10.55
APLC-2.5 ΔNI	6.88	12.26	47.33

Ag_{Prot} coating degrades the NI at the IWA by a factor of 5 greater than the Al_{eLiF} coating for the APLC-3.5 design, and a factor of 7 greater than the Al_{eLiF} coating for the APLC-2.5 design.

Due to the higher nominal contrast, the APLC-2.5 design suffers more from polarization aberration, maximizing at $\sim 2.7 \times 10^{-10}$ at the IWA with Ag_{Prot}. The APLC-3.5 design's maximum degradation in NI also occurs at the IWA at $\sim 10.5 \times 10^{-10}$, but this is within an order of magnitude of the nominal NI. The aluminum-based Al_{eLiF} and Al_{HST} coatings appear to have the better performance than Ag_{Prot}. The greater NI degradation by the Ag_{Prot} coating is likely a function of the higher number of dielectric layers than the aluminum-based coatings. The results in Figs. 7 and 8 are a combination of the common and polarization-dependent aberration modes present in the system and are not representative of the final image plane. What we are most interested in understanding is the final uncorrectable wavefront error, which could limit observations of faint exoplanets at small angular separations.

4 Wavefront Control on Split-Polarization Coronagraphs

In Sec. 3, we consider the polarization aberrations for a static optical system without any ability to minimize the wavefront error. In reality, coronagraphs are active systems equipped with WFSC. The deformable mirror system is capable of performing some degree of correction over the complex wavefront. The 6MST coronagraph features a two-DM system, which is capable of both amplitude and phase correction. In the small aberration regime ($\phi \ll \lambda$), we consider that a DM in the pupil plane modifies only the imaginary component of the field, as shown in Eq. (9)

$$e^{i\phi_{DM}} \approx 1 + i\phi_{DM}. \tag{9}$$

Pueyo et al.[38] and Give'on et al.[39] showed that, through free-space propagation, the out-of-pupil DM2 is capable of applying both real and imaginary modifications to the complex electric field. The combination of an in-pupil DM1 and out-of-pupil DM2 can then provide simultaneous control of amplitude and phase over a 360-deg dark hole. The mathematics for two-DM wavefront control are reviewed in brief in Appendix D.

We know from prior studies[9,10] that there is generally no solution that completely nulls polarization aberrations because their amplitudes and phases tend to have different magnitudes and signs (this is also apparent in Fig. 6). Therefore, in the absence of a polarizing filter, the average complex wavefront of the individual Jones pupil elements J_{avg} must be corrected, as shown in Eq. (10)

$$J_{\text{avg}} = \frac{1}{4}\sum_{j=1}^{2}\sum_{k=1}^{2} J_{j,k}, \tag{10}$$

where j and k are the row and column indices of the Jones pupil $\mathbf{J}$, respectively. In reality, the DM surfaces DM1 and DM2 are solved iteratively using focal plane wavefront sensing and control algorithms, such as pairwise probing and electric field conjugation.[39] However, in the case of the split-polarization coronagraph model for 6MST, we can perform wavefront control on just the x- or y-polarized elements of the Jones pupil separately. This leaves only the cross-terms of the Jones pupil, which add incoherently to the dark hole and tend to be of smaller magnitude.[2] The split-channel method decreases the effort required on the wavefront control system for each channel. The results of applying this correction are shown in Figs. 9 and 10 for the x- and y-polarized channel, respectively. The 2D focal planes for these data are available in Appendix D. We observe substantial improvements in the focal plane intensity across all cases of around an order of magnitude. For the APLC-2.5 coronagraph, the maximum NI degradation occurs in the x-polarized channel for the HST coating at roughly 1.19×10^{-11} at $2.5\lambda/D$. The other coatings (Ag_{Prot}, Al_{eLiF}) maximize near 7×10^{-12} at the IWA, with the pAg coating performing the best. The NI profiles are generally higher for the APLC-3.5, but this is a feature of its higher nominal NI, as discussed in Sec. 3. The maximum NI degradation occurs again with the Al_{HST} coating at roughly 8.13×10^{-11} for the APLC-3.5 design. The other coatings maximize near 6×10^{-11}. For both coronagraph designs, the performance degradation is nearly identical across the x- and

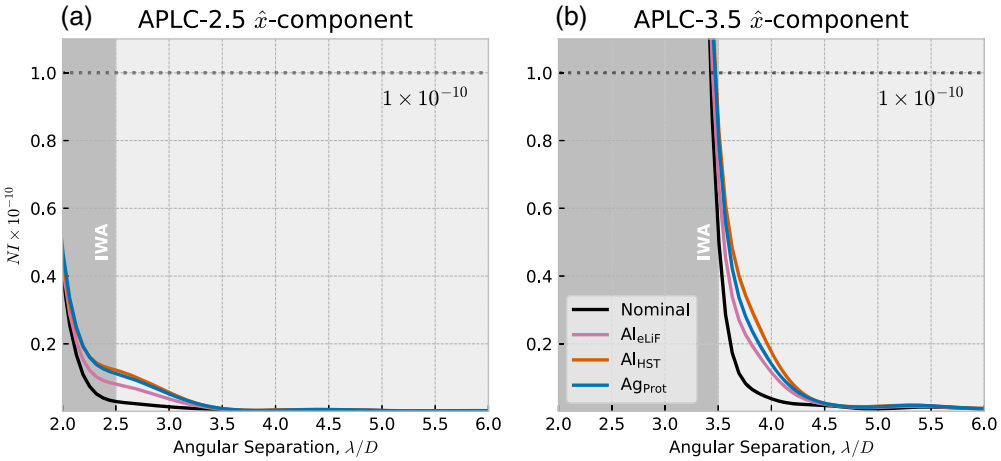

Fig. 9 Azimuthally averaged radial profiles for the x-polarized coronagraph channel using the APLC-2.5 (a) and APLC-3.5 (b). The influence of the polarization aberrations on the final focal plane is approximately constant for both coronagraphs. The Al_{HST} coating leaves the largest amount of polarization aberration, and the Al_{eLiF} and Ag_{Prot} coatings leave the least with the contrast degraded by roughly a factor of 2 at the IWA. This is particularly encouraging for UV science with the HWO, which requires a coating like Al_{eLiF} to achieve appreciable transmission in the UV.

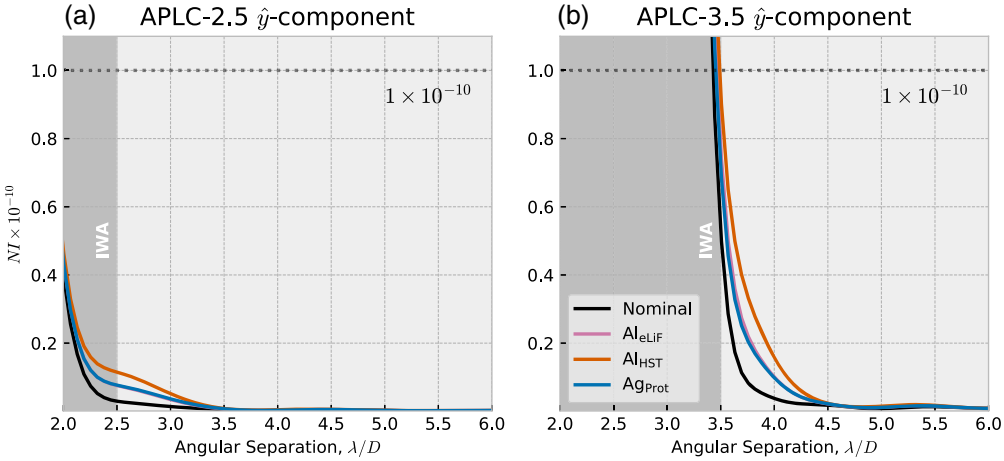

Fig. 10 Azimuthally averaged radial profiles for the *y*-polarized coronagraph channel using the APLC-2.5 (a) and APLC-3.5 (b). These curves show very similar trends to the *x*-polarized channel across the coronagraphs and coatings, with the exception of the Ag_{Prot} coating, which has slightly better performance in *y*-polarization.

y-polarized channels, indicating that there is not a strong preference for one polarization state imposed by the telescope geometry.

We find from these data that the coronagraphic performance limited by polarization aberration residuals is predicted by the retardance curve in Fig. 5. The Al_{HST} coating leaves the worst residuals, then the Al_{eLiF} coating, and then the Ag_{Prot} coating. For both polarization channels, no cases exceed an NI of 1×10^{-10} at the IWA. However, the Al_{HST} coating for the APLC-3.5 coronagraph approaches this value. Given the static nature of polarization aberrations, this degradation can be partially removed through post-processing. The coatings may age over time, and their refractive indices may vary, changing the polarization aberrations. However, this change occurs over very long timescales and would not limit any single observation. Consequently, the post-processing gains seen by implementing PSF subtraction routines such as Karhunen–Loeve image projection[40] or non-negative matrix factorization (NMF)[41] could eliminate the remaining polarized residuals.

5 Discussion and Future Work

In this work, we analyze and assess the polarization aberrations present in JPL's 6MST optical design and coronagraph to determine their ultimate influence on APLC's that are nominally capable of imaging at 10^{-10} NI. We study several coating equations, including the Al_{eLiF} coating that is being considered for the HWO to enable science in the UV. Our analysis suggests that the nominal wavefront error from polarization aberrations in the Ag_{Prot} coating results in NI degradation at the level of 10×10^{-10} at the IWA, whereas the nominal aberration from the aluminum-based coatings is better at about a factor of 5 lower. We also show that splitting the coronagraph into orthogonal *x*- and *y*-polarized channels and applying wavefront control can reduce the residuals by an order of magnitude, with an un-correctable floor at the IWA at around four times the nominal NI for the APLC-2.5 and two times the nominal NI for the APLC-3.5. Being within a factor of 2 to 4 is not in principle punishing when trying to evaluate sensitivity at the IWA. For example, Douglas et al.[42] quoted a post-processing attenuation factor of ≈0.25 for the Roman Coronagraph's HLC mode using Roman's Observing Scenario 9 dataset and NMF[42] to subtract the coronagraphic PSF. Of course, other deleterious effects will further complicate the ability to isolate and mitigate polarization aberrations. Jitter and stellar diameter cause leakage in the same region in the focal plane as polarization aberrations. Having this compounded stellar leakage be polarized could be problematic to correct with WFSC. Krist et al.[43] showed in numerical modeling efforts for HabEx that the combination of polarization, stellar diameter, and optical surface errors degrade the contrast at the IWA of the HabEx coronagraph to $10^{-10} - 10^{-9}$.

To better understand this effect, polarization aberrations should be considered in future models that include stellar diameter and jitter.

Given that aluminum-based coatings are the scientific community's strong preference for HWO to enable UV science,[44] we must carefully consider their contribution to polarization aberrations going forward. In this study, we observe that the polarization aberrations from aluminum-based coatings contribute less to the total wavefront error budget than the silver-based coating we studied with multiple dielectric layers. Furthermore, based on our results in Figs. 9 and 10, Al_{eLiF} is correctable to within a factor of 2 of the nominal NI for both coronagraph designs. Understanding how this performance changes, particularly at shorter wavelengths where polarization aberrations are known to be greater[9,10] is a critical next step in this work. Should polarization aberrations be more limiting at shorter wavelengths, compensation strategies should be considered.

5.1 Compensation Strategies

To achieve the sensitivity required for the Habitable Worlds Observatory, conducting trade studies that jointly consider the telescope and coronagraph is essential. One such path forward to mitigate the polarization aberrations in the coronagraph is to optimize the coating layer thicknesses in the OTA to minimize the diattenuation and retardance contributed by the telescope. This is a problem that requires input from all onboard instruments and consequently may be over constrained but could severely mitigate the polarization aberrations from the OTA. An alternative is to optimize the layer thicknesses of the optics internal to the coronagraph. Although each optic may not have a large contribution to the overall polarization aberrations, in the split-coronagraph model presented in this work, the coatings could be optimized for a given polarization channel. The integrated open-source modeling method we present in this study was designed for such a task. Poke's ability to directly link PRT models to open-source diffraction models means that a thin-film optimization can be done in a Python environment, and the contrast can be evaluated at every iteration.

Other paths forward could consider emerging technologies that require maturation to be suitable for HWO. Miller et al.[45] showed that leveraging the birefringence from a liquid crystal negative C-plate could compensate for the retardance from aluminum reflections, and a thin-film fluoropolymer could compensate for the diattenuation. They demonstrated this compensation over a broad spectral bandwidth (470 to 600 nm). This film could be deposited on an internal coronagraph optic to compensate for some of the polarization aberrations accrued in the OTA. Metasurfaces are another emerging technology that has seen substantive development for simultaneous control of phase and amplitude. Rubin et al.[46] illustrated in their exhaustive review of the technology that metasurfaces enable spatially varying polarization optics. Li et al.[47] leveraged this capability to construct a polarization grating that enabled full-Stokes polarimetry in a single image. In the Jones matrix representation of a metasurface,[46] designing a metasurface device that minimizes the retardance present in a Jones pupil is in principle a simple optimization problem. However, metasurfaces can be designed to generate prescribed amplitude and phase distributions in the far field using an iterative transform algorithm.[48] Metasurfaces have not seen substantive implementation in high-contrast imaging and should be considered for systems sensitive to polarization aberrations such as the HWO.

6 Appendix A: Forward and Adjoint Model for an Apodized Pupil Lyot Coronagraph

Using the reverse-mode algorithmic differentiation rules from Jurling and Fienup,[20] we construct the forward and adjoint model of the APLC operator on an incident scalar field. The forward model is given on the left of Table 6 and tells us how the incident field is related to the target dark hole T. The adjoint model is given on the right of Table 6 and tells us the gradient of the cost function [$\mathcal{L}$ in Eq. (7)] with respect to the pixel values in the apodizer. The conventions used for these operators are shown in Table 7. Note that although we refer to the algorithm derived below as "novel" in Sec. 1, the design of coronagraph masks with gradient back-propagation logic is not novel. Several investigators have employed the use of Python packages that support automatic differentiation. Wong et al.[49] illustrated a Jax-backed optical propagator called morphine (which

Table 6 Steps to compute the forward propagation of the APLC from the grayscale apodizer values (a) to the loss function $\mathcal{L}$ and the corresponding adjoint model derived by reverse-mode algorithmic differentiation.

Forward	Adjoint
$b = \mathcal{R}[a]$	$\overline{a} = \mathcal{R}[\overline{b}]$
$B = \mathrm{FT}[b]$	$\overline{b} = \mathrm{IFT}[\overline{B}]$
$C = B \circ \mathrm{FPM}$	$\overline{B} = (\mathrm{FPM})^* \circ \overline{C}$
$c = \mathrm{FT}[C]$	$\overline{C} = \mathrm{IFT}[\overline{c}]$
$d = c \circ \mathrm{LS}$	$\overline{c} = (\mathrm{LS})^* \circ \overline{d}$
$D = \mathrm{FT}[d]$	$\overline{d} = \mathrm{IFT}[\overline{D}]$
$I = \lvert D \rvert^2$	$\overline{D} = 2\overline{I} \circ D$
$\mathcal{L} = (I - T)^2$	$\overline{I} = 2(I - T)$

Table 7 Conventions used in the algorithmic differentiation model for this study.

Symbol	Description
$\circ$	Elementwise multiplication
$*$	Complex conjugate
a	Variables used in optimization, i.e., the pixel value in apodizer
FPM	Coronagraph focal plane mask operator
LS	Coronagraph Lyot stop operator
$\mathrm{FT}[a]$	Fourier transform of a
$\mathrm{IFT}[a]$	Inverse Fourier transform of a
$\mathcal{R}[a]$	Real part of a
$\overline{a}$	$\frac{\partial}{\partial a}\mathcal{L}$, partial derivative of loss function with respect to a

has since been adapted into ∂Lux[50]), which can be used to design an apodizing phase plate coronagraph. Por et al.[51] demonstrated the design of APLCs using Tensorflow to perform the automatic differentiation. Performing the differentiation "by hand" and coding the backpropagation rules explicitly has the potential for greater versatility, rather than relying on the backpropagation engines of packages such as Jax or Tensorflow. The explicit backpropagation has the potential for lower runtimes because no additional calculations need to be done to determine the gradient of the objective function. However, this approach becomes more difficult to implement as the complexity of the forward model increases.

7 Appendix B: Jones Pupils for Other Coating Studies

The Jones pupils for the remaining $\mathrm{Al}_{\mathrm{HST}}$ and $\mathrm{Ag}_{\mathrm{Prot}}$ coatings are included here in Figures 11 and 12, respectively. We observe a similar amplitude and phase distribution between the $\mathrm{Al}_{\mathrm{eLiF}}$ coating in Figure 6 and the $\mathrm{Al}_{\mathrm{HST}}$ coating in Fig. 11, likely due to the similarities in the coating formulae. The $\mathrm{Ag}_{\mathrm{Prot}}$ coating in Fig. 12 has a similar amplitude distribution to the other two Jones pupils studied, but the phase distribution differs more significantly.

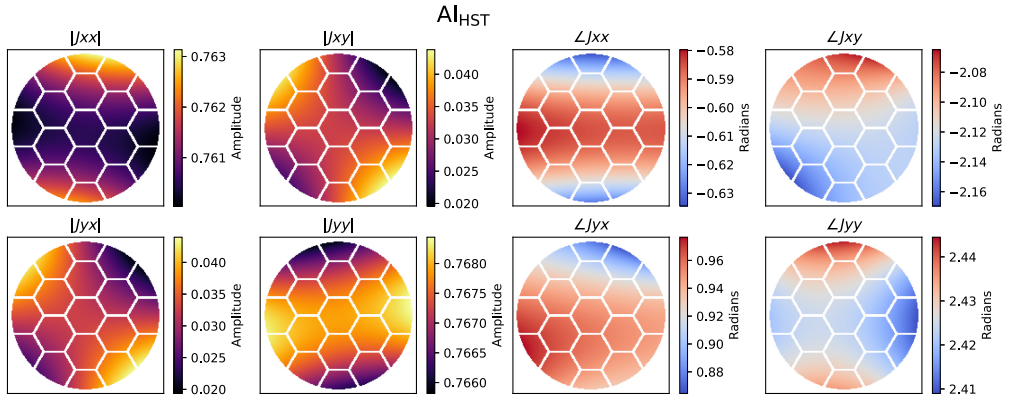

Fig. 11 Uncompensated Jones pupil for the Al$_{HST}$ coating.

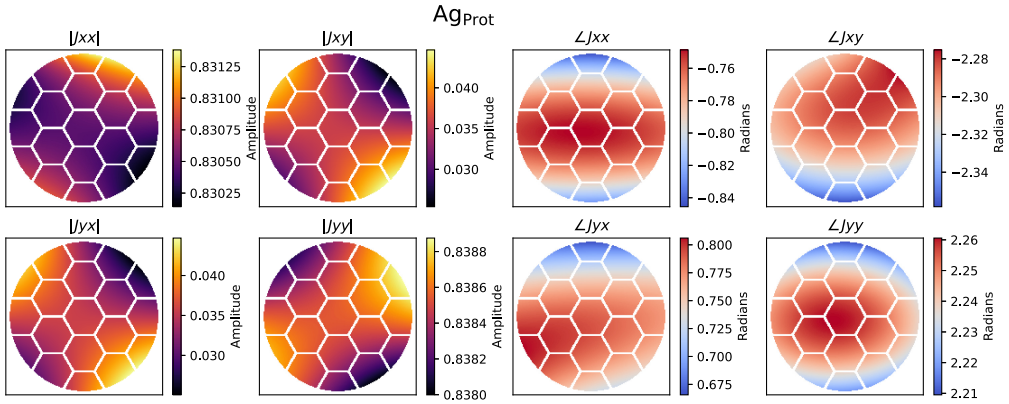

Fig. 12 Uncompensated Jones pupil for the Ag$_{Prot}$ coating.

8 Appendix C: Coronagraphic Focal Planes for the Split Polarization Channels

Figures 13 and 14 show the coronagraphic focal planes for the APLC's designed in this study subject to the polarization aberrations after splitting the coronagraph into orthogonal polarization states. While a majority of the focal plane degradation present in Fig. 7 has disappeared, a non-zero amount of degradation remains at the inner working angle. This pattern is indicative of the

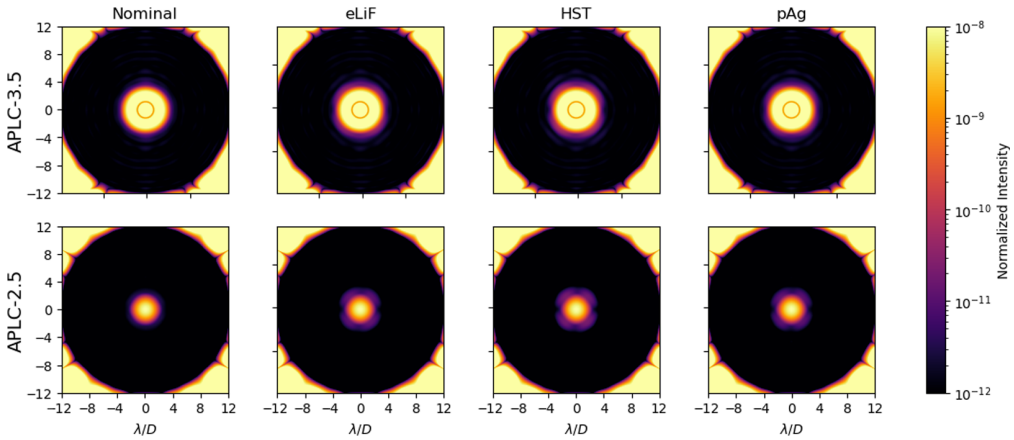

Fig. 13 Compensated coronagraphic focal planes using the *x*-polarized channel of the split 6MST coronagraph.

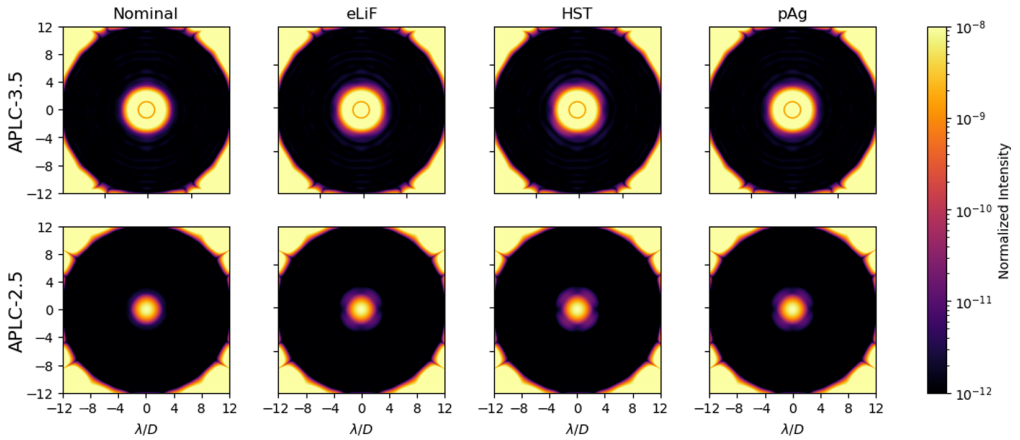

Fig. 14 Compensated coronagraphic focal planes using the *y*-polarized channel of the split 6MST coronagraph.

"Maltese Cross", which is characteristic of polarization aberrations of astronomical telescopes that arises from the off-diagonal term in the Jones pupil.

9 Appendix D: Review of 2-DM Wavefront Control

The propagation from the field after the in-pupil DM1 to the out-of-pupil DM2 can be represented with Fresnel propagation of the field at DM2 to DM1, given by the P_{21} operator in Eq. (11)

$$P_{21}[\phi_{DM2}] = \phi_{DM2} * \frac{1}{i\lambda z_{21}} \exp\left(\frac{i\pi}{\lambda z_{21}}(x^2+y^2)\right), \tag{11}$$

where $*$ is the convolution operator and z_{21} is the distance from DM2 to DM1. Following Give'on et al.,[39] the total field at the coronagraph focal plane (E_{coro}) in the small perturbation approximation is given by Eq. (12)

$$E_{\text{coro}} \approx C[\alpha + i\beta] + iC[P_{21}[\phi_{DM2}]] + iC[\phi_{DM1}], \tag{12}$$

where α and β are the real and imaginary components of an arbitrary aberration, respectively, and C is the linear coronagraph propagation operator that represents the propagation from the entrance pupil to the focal plane of the coronagraph. Through the Fresnel propagation, DM2 has control over both the real and imaginary parts of the electric field, and DM1 has control over the imaginary part of the electric field. In this formulation, we can consider the correction applied by DM2 to be a rotation on the complex plane such that the field at DM1 is imaginary only. The correction applied by DM1 is then able to conjugate the resulting imaginary-only field for complete correction of phase and amplitude.

Disclosures

The authors declare that there are no financial interests, commercial affiliations, or other potential conflicts of interest that could have influenced the objectivity of this research or the writing of this paper.

Code and Data Availability

This research primarily made use of the following open-source software packages: Poke,[17] prysm,[52] and dygdug,[21] all of which can be found on their associated GitHub repositories. The refractive index information was retrieved from refractiveindex.info, with interpolated index models created in Poke for easy use. The remaining files in this paper (i.e., coronagraph masks, PSF simulations, propagation models) can be provided upon reasonable request.

Acknowledgments

This research made use of several open-source Python packages, including POPPY,[53] HCIPy,[54] prysm,[52] numpy,[55] matplotlib,[56] ipython,[57] astropy,[58–60] cupy,[61] and scipy.[62] This work was supported by a NASA Space Technology Graduate Research Opportunity. This study utilized high-performance computing (HPC) resources supported by the University of Arizona TRIF, UITS, and Research, Innovation, and Impact (RII) and maintained by the UArizona Research Technologies department. A portion of this research was carried out at the Jet Propulsion Laboratory, California Institute of Technology, under a contract with the National Aeronautics and Space Administration (Grant No. 80NM0018D0004). J.N.A was in part supported by NASA through the NASA Hubble Fellowship grant #HST-HF2-51547.001-A awarded by the Space Telescope Science Institute, which is operated by the Association of Universities for Research in Astronomy.

References

1. B. Mennesson et al., "The Roman Space Telescope coronagraph technology demonstration: current status and relevance to future missions," *Proc. SPIE* **12180**, 121801W (2022).
2. J. E. Krist et al., "End-to-end numerical modeling of the Roman Space Telescope coronagraph," *J. Astron. Telesc. Instrum. Syst.* **9**(4), 045002 (2023).
3. D. Redding et al., "Integrated active control of coronagraph and telescope for high contrast imaging," *Proc. SPIE* **12680**, 126801M (2023).
4. J. B. Breckinridge, W. S. T. Lam, and R. A. Chipman, "Polarization aberrations in astronomical telescopes: the point spread function," *Publ. Astron. Soc. Pacif.* **127**, 445 (2015).
5. J. P. McGuire and R. A. Chipman, "Polarization aberrations. 1. Rotationally symmetric optical systems," *Appl. Opt.* **33**, 5080–5100 (1994).
6. J. P. McGuire and R. A. Chipman, "Polarization aberrations. 2. Tilted and decentered optical systems," *Appl. Opt.* **33**, 5101–5107 (1994).
7. J. Sasián, "Polarization fields and wavefronts of two sheets for understanding polarization aberrations in optical imaging systems," *Opt. Eng.* **53**(3), 035102 (2014).
8. B. S. Gaudi et al., "The habitable exoplanet observatory (HabEx) mission concept study final report," https://arxiv.org/abs/2001.06683 (2020).
9. S. D. Will and J. R. Fienup, "Effects and mitigation of polarization aberrations in LUVOIR coronagraph," *Proc. SPIE* **11117**, 1111710 (2019).
10. R. M. Anche et al., "Polarization aberrations in next-generation giant segmented mirror telescopes (GSMTs): effect on the coronagraphic performance," *Astron. Astrophys.* **672**, A121 (2023).
11. K. Balasubramanian et al., "Polarization compensating protective coatings for TPF-Coronagraph optics to control contrast degrading cross polarization leakage," *Proc. SPIE* **5905**, 59050H (2005).
12. G. Yun, K. Crabtree, and R. A. Chipman, "Three-dimensional polarization ray-tracing calculus I: definition and diattenuation," *Appl. Opt.* **50**, 2855–2865 (2011).
13. G. Yun, S. C. McClain, and R. A. Chipman, "Three-dimensional polarization ray-tracing calculus II: retardance," *Appl. Opt.* **50**, 2866–2874 (2011).
14. R. A. Chipman, W.-S. T. Lam, and G. Young, *Polarized Light and Optical Systems*, CRC Press (2018).
15. N. Clark and J. B. Breckinridge, "Polarization compensation of Fresnel aberrations in telescopes," *Proc. SPIE* **8146**, 81460O (2011).
16. R. Belikov et al., "Coronagraph design survey for future exoplanet direct imaging space missions: interim update," *Proc. SPIE* **12680**, 126802G (2023).
17. J. N. Ashcraft et al., "Poke: an open-source, ray-based physical optics platform," *Proc. SPIE* **12664**, 1266404 (2023).
18. A. J. E. Riggs et al., "Flight mask designs of the Roman Space Telescope coronagraph instrument," *Proc. SPIE* **11823**, 118231Y (2021).
19. R. Juanola-Parramon et al., "Modeling and performance analysis of the LUVOIR coronagraph instrument," *J. Astron. Telesc. Instrum. Syst.* **8**(3), 034001 (2022).
20. A. S. Jurling and J. R. Fienup, "Applications of algorithmic differentiation to phase retrieval algorithms," *J. Opt. Soc. Am. A* **31**, 1348–1359 (2014).
21. B. Dube and J. N. Ashcraft, "dygdug," https://github.com/brandondube/dygdug (2023).
22. J. Nocedal, "Updating quasi-newton matrices with limited storage," *Math. Comput.* **35**(151), 773–782 (1980).
23. J. Morales and J. Nocedal, "Remark on "algorithm 778: L-bfgs-b: Fortran subroutines for large-scale bound constrained optimization"," *ACM Trans. Math. Softw.* **38**, 1–4 (2011).
24. P. Martinez et al., "Design, analysis, and testing of a microdot apodizer for the Apodized Pupil Lyot Coronagraph," *Astron. Astrophys.* **495**(1), 363–370 (2009).

25. J. Llop-Sayson et al., "High-contrast demonstration of an apodized vortex coronagraph," *Astron. J.* **159**, 79 (2020).
26. D. Rouan, *Coronagraphy*, Springer, Berlin (2011).
27. B. Fleming et al., "Advanced environmentally resistant lithium fluoride mirror coatings for the next generation of broadband space observatories," *Appl. Opt.* **56**, 9941–9950 (2017).
28. J. Peatross and M. Ware, "Physics of light and optics," https://optics.byu.edu (2015).
29. H. H. Li, "Refractive index of alkali halides and its wavelength and temperature derivatives," *J. Phys. Chem. Ref. Data* **5**, 329–528 (1976).
30. L. V. R. de Marcos et al., "Self-consistent optical constants of MgF_2, LaF_3, and CeF_3 films," *Opt. Mater. Express* **7**, 989–1006 (2017).
31. L. Gao, F. Lemarchand, and M. Lequime, "Refractive index determination of SiO_2 layer in the UV/VIS/NIR range: spectrophotometric reverse engineering on single and bi-layer designs," *J. Eur. Opt. Soc. Rapid Publ.* **8**, 13010 (2013).
32. L. Gao, F. Lemarchand, and M. Lequime, "Exploitation of multiple incidences spectrometric measurements for thin film reverse engineering," *Opt. Express* **20**, 15734–15751 (2012).
33. H. R. Philipp, "Optical properties of silicon nitride," *J. Electrochem. Soc.* **120**, 295 (1973).
34. F. Cheng et al., "Epitaxial growth of atomically smooth aluminum on silicon and its intrinsic optical properties," *ACS Nano* **10**, 9852–9860 (2016).
35. A. Ciesielski et al., "Controlling the optical parameters of self-assembled silver films with wetting layers and annealing," *Appl. Surf. Sci.* **421**, 349–356 (2017).
36. I. H. Malitson, "Interspecimen comparison of the refractive index of fused silica," *J. Opt. Soc. Am.* **55**, 1205–1209 (1965).
37. H. Fujiwara, *Appendix 4: Jones-Mueller Matrix Conversion*, John Wiley and Sons, Ltd (2007).
38. L. Pueyo et al., "Optimal dark hole generation via two deformable mirrors with stroke minimization," *Appl. Opt.* **48**, 6296–6312 (2009).
39. A. Give'on et al., "Broadband wavefront correction algorithm for high-contrast imaging systems," *Proc. SPIE* **6691**, 66910A (2007).
40. J. J. Wang et al., "pyKLIP: PSF subtraction for exoplanets and disks," Astrophysics Source Code Library, record ascl:1506.001 (2015).
41. B. Ren et al., "Non-negative matrix factorization: robust extraction of extended structures," *Astrophys. J.* **852**, 104 (2018).
42. E. S. Douglas et al., "Sensitivity of the Roman Coronagraph instrument to exozodiacal dust," *Publ. Astron. Soc. Pacif.* **134**, 024402 (2022).
43. J. Krist et al., "Numerical modeling of the Habex coronagraph," *Proc. SPIE* **11117**, 1111705 (2019).
44. P. Scowen, "General astrophysics needs and coronagraphy," Starlight Suppression Workshop, https://exoplanets.nasa.gov/internal_resources/2808/Aug082023_0900_Scowen-Towards-Starlight-Suppression-Workshop.pdf (2023).
45. S. Miller, L. Jiang, and S. Pau, "Birefringent coating to remove polarization aberrations," *Opt. Express* **30**, 20629–20646 (2022).
46. N. A. Rubin, Z. Shi, and F. Capasso, "Polarization in diffractive optics and metasurfaces," *Adv. Opt. Photonics* **13**(4), 836–970 (2022).
47. L. W. Li et al., "Evaluation and characterization of imaging polarimetry through metasurface polarization gratings," *Appl. Opt.* **62**, 1704–1722 (2023).
48. N. A. Rubin et al., "Jones matrix holography with metasurfaces," *Sci. Adv.* **7**(33), eabg7488 (2021).
49. A. Wong et al., "Phase retrieval and design with automatic differentiation: tutorial," *J. Opt. Soc. Am. B* **38**, 2465–2478 (2021).
50. L. Desdoigts et al., "Differentiable optics with ∂Lux: I-deep calibration of flat field and phase retrieval with automatic differentiation," *J. Astron. Telesc. Instrum. Syst.* **9**(2), 028007 (2023).
51. E. H. Por, L. Pueyo, and R. Soummer, "Joint optimization of multiple optical planes in a stellar coronagraph," *Proc. SPIE* **12180**, 121805J (2022).
52. B. D. Dube et al., "Exascale integrated modeling of low-order wavefront sensing and control for the Roman Coronagraph instrument," *J. Opt. Soc. Am. A* **39**, C133–C142 (2022).
53. M. Perrin et al., "POPPY: physical optics propagation in Python," Astrophysics Source Code Library, record ascl:1602.018 (2016).
54. E. H. Por et al., "High contrast imaging for python (HCIPy): an open-source adaptive optics and coronagraph simulator," *Proc. SPIE* **10703**, 1070342 (2018).
55. C. R. Harris et al., "Array programming with NumPy," *Nature* **585**, 357–362 (2020).
56. J. D. Hunter, "Matplotlib: a 2D graphics environment," *Comput. Sci. Eng.* **9**(3), 90–95 (2007).
57. F. Pérez and B. E. Granger, "IPython: a system for interactive scientific computing," *Comput. Sci. Eng.* **9**, 21–29 (2007).

58. Astropy Collaboration et al., "Astropy: a community Python package for astronomy," *Astron. Astrophys.* **558**, A33 (2013).
59. Astropy Collaborationet al., "The astropy project: building an open-science project and status of the v2.0 core package," *Astron. J.* **156**, 123 (2018).
60. Astropy Collaboration et al., "The astropy project: sustaining and growing a community-oriented open-source project and the latest major release (v5.0) of the core package," *Astrophys. J.* **935**, 167 (2022).
61. R. Okuta et al., "CuPy: a NumPy-compatible library for NVIDIA GPU calculations," in *Proc. Workshop Mach. Learn. Syst. (Learning Sys) in the 31st Annu. Conf. Neural Inf. Process. Syst. (NIPS)* (2017).
62. P. Virtanen et al., "SciPy 1.0: fundamental algorithms for scientific computing in Python," *Nat. Methods* **17**, 261–272 (2020).

Jaren Nicholas Ashcraft (he/his) is a NASA Hubble Fellow at UC Santa Barbara. He received his PhD in optical sciences at the University of Arizona's Wyant College of Optical Sciences working with the UA Space Astrophysics Laboratory and Large Optics Fabrication and Testing Group. He received his BS degree in optical engineering from the University of Rochester in 2019 and his MS degree in optical sciences from the University of Arizona in 2022. He was a recipient of a NASA Space Technology Graduate Research Opportunities award.

Brian Monacelli is a principal optical engineer and technical group supervisor at Jet Propulsion Laboratory, where he led the optical assembly and alignment of the Coronagraph Instrument for the Roman Space Telescope and the SHERLOC Instrument of the Mars2020 Perseverance Rover, among other optical instruments. He received his BS degree in applied optics from the Rose-Hulman Institute of Technology, his MS degree in optics from the University of Rochester, and his PhD in optics from the University of Central Florida/CREOL. He writes applied curricula that teach technicians to learn hands-on laboratory skills via the Pasadena City College Laser Technology program. He also serves on the Optics and Electro-Optics Standards Council, where he supports the development of optics standards.

Biographies of the other authors are not available.